Geochemistry, Geophysics, Geosystems

RESEARCH ARTICLE
10.1029/2018GC007850

Key Points:
- A new strategy for acquisition and processing of combined elemental and U-Pb isotopic data for carbonate U-Pb geochronology is presented
- Image maps of time-resolved analyses allow straightforward visual assessment of data in combination with structural and textural features
- Selection and pooling of pixels from image maps assists in extraction of accurate and precise U-Pb ages from likely homogeneous age domains

Supporting Information:
- Supporting Information S1
- Data Set S1

Correspondence to:
K. Drost,
drostk@tcd.ie

Citation:
Drost, K., Chew, D., Petrus, J. A., Scholze, F., Woodhead, J. D., Schneider, J. W., & Harper, D. A. T. (2018). An image mapping approach to U-Pb LA-ICP-MS carbonate dating and applications to direct dating of carbonate sedimentation. *Geochemistry, Geophysics, Geosystems*, *19*. https://doi.org/10.1029/2018GC007850

Received 24 JUL 2018
Accepted 22 NOV 2018
Accepted article online 28 NOV 2018

An Image Mapping Approach to U-Pb LA-ICP-MS Carbonate Dating and Applications to Direct Dating of Carbonate Sedimentation

Kerstin Drost[1], David Chew[1], Joseph A. Petrus[2], Frank Scholze[3], Jon D. Woodhead[2], Joerg W. Schneider[3], and David A. T. Harper[4]

[1]Department of Geology, Trinity College Dublin, Dublin, Ireland, [2]School of Earth Sciences, The University of Melbourne, Melbourne, Victoria, Australia, [3]Technische Universität Bergakademie Freiberg, Geological Institute, Freiberg, Germany, [4]Palaeoecosystems Group, Department of Earth Sciences, Durham University, Durham, UK

Abstract We present a new approach to laser ablation inductively coupled plasma mass spectrometry (LA-ICP-MS) U-Pb dating of carbonates based on selection and pooling of pixels from 2-D elemental and isotopic ratio maps. This image mapping technique is particularly useful for targeting subdomains in samples with complex geological histories. Key major and trace elements that are sensitive to detrital components, postformational fluid ingress, mineralogical changes, or diagenetic overprinting are measured along with the Pb and U isotopic data. Laser sampling is undertaken along successive linear rasters that are compiled into maps using the *Monocle* add-on for *Iolite*, with one pixel in the map corresponding to one time slice of the time-resolved signal. These element, element ratio, and isotope ratio maps can be overlain over photomicrographs or scanning electron microscopy images to spatially link compositional data to textural and structural features. The pixels corresponding to likely homogeneous age domains can be isolated by applying appropriate selection criteria (e.g., Th $<$ 0.3 ppm, Mg/Ca $<$ 0.004) and pooled into pseudo-analyses using a proxy for the parent/daughter ratio (e.g., $^{207}Pb/^{235}U$, $^{238}U/^{208}Pb$) to retrieve the largest possible spread of the data points on isochron diagrams. The approach is best suited for analytical setups capable of rapidly or simultaneously scanning over a large mass range and can yield a precision of ±1% or better on quadrupole instruments depending on U concentration, $^{238}U/^{204}Pb$, and age of the sample. The sample-specific filtering criteria for selection and rejection of data and their rationale can be reported, resulting in more transparency with regard to data processing.

Plain Language Summary Carbonate minerals (the constituents of limestones, carbonate veins, and certain fossil shells) form in different environments and in response to different geological processes. Based on the radioactive decay of uranium to lead, the timing of these processes can be dated by measuring uranium and lead isotopes in carbonate minerals. However, this is often difficult to achieve because the uranium-lead isotope system in carbonates is readily disturbed by later processes or events. Problems also arise if carbonate rocks contain detrital material or different generations of carbonate minerals or if they have unfavorable lead-uranium ratios. Our approach to dating of carbonates involves mapping of polished rock fragments for key elements along with uranium and lead isotopes. The elemental and isotope maps can be precisely overlain over photomicrographs and other images to link the analytical data to textural and structural features of the sample. Pixels corresponding to specific chemical criteria can be selected from the maps to target areas that share likely similar formation conditions and age. Pooling of the selected pixels in pseudo-analyses retrieves the largest possible spread in uranium-lead ratios and helps improve the precision of the age. The approach assists in deriving and interpreting age information from complex carbonate samples.

1. Introduction

Direct dating of calcite and other carbonate minerals using the U-Pb system is an important tool to constrain the timing of processes such as carbonate deposition during key intervals of Earth history, carbonate diagenesis, metamorphism, fault activity, hydrothermal mineralization, and ancient weathering episodes (e.g., Babinski et al., 1995; Denniston et al., 2008; Godeau et al., 2018; Hill et al., 2016; Hoff et al., 1995; Jahn, 1988; Moorbath et al., 1987; Rasbury et al., 1998; Rasbury & Cole, 2009; Ring & Gerdes, 2016; Smith et al., 1991; Wang et al., 1998; Woodhead et al., 2010). Important prerequisites to the successful U-Pb

dating of carbonates are a closed isotopic system, a homogeneous initial ("common") Pb composition, and a sufficient spread in the parent/daughter ratio. However, low U concentrations and/or high amounts of initial Pb as well as (local) open system behavior of the U-Pb system, or the presence of different generations of carbonate minerals, often hinder the extraction of reliable age information. Recent experiments with carbonate U-Pb dating using the laser ablation inductively coupled plasma mass spectrometry technique (LA-ICP-MS) (e.g., Burisch et al., 2017; Hansman et al., 2018; Li et al., 2014; Nuriel et al., 2017; Pagel et al., 2018; Ring & Gerdes, 2016; Roberts & Walker, 2016) have already shown great potential compared to bulk rock isotope dilution (ID) approaches in overcoming some of these issues. In particular, they provide the ability to identify portions of the sample that have high U concentrations and/or high $^{238}U/^{204}Pb$ ratios and therefore assist in retrieving the largest possible spread in parent/daughter ratios. However, due to typically low U and radiogenic Pb concentrations in carbonates, large spot sizes are required during U-Pb LA-ICP-MS carbonate analysis (85 to 235 μm; e.g., Godeau et al., 2018; Hansman et al., 2018; Nuriel et al., 2017; Ring & Gerdes, 2016; Roberts et al., 2017), which make it potentially difficult to avoid alteration zones or the sampling of different generations of carbonate minerals. Furthermore, as emphasized by Rasbury and Cole (2009), the systems in which carbonate minerals form can often be complex and long lived, and, therefore, the question arises as to what geological "event" is actually being dated.

To reduce the impact of these limitations, we describe a new approach based around LA-ICP-MS rastering to generate image maps not only for U/Pb isotope data but also for key major and trace elements that are sensitive to detrital components, postformational fluid ingress, mineralogical changes, or diagenetic overprinting. These elemental or isotopic image maps can be precisely overlain over other images, such as photomicrographs and scanning electron microscopy (SEM) images, to spatially link U-Pb data to compositional, textural, and structural features. After careful inspection of these features and the elemental compositions, pixels corresponding to particular criteria can be selected from a 2-D map and pooled into pseudo-analyses (hereafter referred to as "analyses") using the flexible map interrogation tool Monocle (Petrus et al., 2017)—an add-on for the mass spectrometric data reduction software package Iolite (Paton et al., 2011). We show here both the advantages and the limitations of this image mapping approach.

2. Samples, Analytical Methods, and Data Processing

2.1. Samples

The image mapping approach is demonstrated on two limestone samples and on a brachiopod shell embedded in micritic limestone.

Sample DBT64 comes from the lacustrine Long Point limestone (Duff Brown Tank locality in the Colorado Plateau, USA) and has yielded a Paleocene depositional age of 64.04 ± 0.67 Ma (2 s) as determined by ID multicollector inductively coupled plasma mass spectrometry (ID-MC-ICP-MS) using the U-Pb system (Hill et al., 2016). Petrographic analyses of hand specimens and thin sections have revealed the presence of variable proportions of secondary calcite cement in the Long Point limestone. However, this late cement phase is minor (<5%) in the rocks from Duff Brown Tank locality (Hill et al., 2016). The secondary calcite was interpreted to have formed during the last 2 Myr and has very low U and relatively high Pb concentrations which results in high Pb/U ratios. Furthermore, the $^{206}Pb/^{204}Pb$ ratio (21.7) of the late cement is similar to the initial $^{206}Pb/^{204}Pb$ value (21.58 ± 0.24) derived from the total Pb/U 3-D isochron ($^{238}U/^{206}Pb$ versus $^{207}Pb/^{206}Pb$ vs. $^{204}Pb/^{206}Pb$) of the primary carbonate. Therefore, Hill et al. (2016) regard the secondary calcite cement not to have a significant impact on the U-Pb ID-MC-ICP-MS date of the whole rock.

The second sample (JS4) is a lacustrine limestone from the uppermost Rothenburg Formation of the Carboniferous-Permian Saale Basin in Germany. The Rothenburg Formation consists of fining-upward cycles of red continental clastic sediments that commonly contain vertisols and calcisols with calcareous rhizoconcretions and calcretes. A decimeter-thick lacustrine limestone developed at the top of the cycle (Gebhardt, 1988; Schneider et al., 2005). This variably gray to red limestone contains ostracods, freshwater gastropods, and characean algae (filamentous green algae that are the closest algal relatives to higher plants) and locally disarticulated vertebrate remains. Lacustrine carbonate precipitation is interpreted to be microbially mediated by calcareous algae in an oligotrophic lake (Gebhardt & Schneider, 1985; Gebhardt, 1988; Schneider et al., 2005). A Stephanian (Kazimovian/Gzhelian) stratigraphic age for the Rothenburg Formation

Table 1
Instrument Settings and Operating Conditions

Laser	Settings
Instrument	Photon Machines Analyte Excite ArF 193 nm excimer
Pulse duration	≤4 ns
Laser carrier gas	0.15 to 0.2 L/min cell He for ARIS, 0.5 L/min for 2-mm ID Teflon tubing 0.25 l/min cup He for ARIS, 0.2 l/min for 2 mm ID teflon tubing
Additional gas	11 ml/min N_2
Washout and background	25 s
Energy density	2.5 J/cm^2
Sampling strategy	Successive linear rasters without overlap
Spot size	47 to 95 μm square
Repetition rate	35 to 40 Hz
Scan speed	20 to 40 μm/s
Inductively coupled plasma mass spectrometry	
Instrument	Agilent 7900, quadrupole
Plasma radio frequency power	1,550 W
Sample gas flow	0.55 L/min

is implied by macroflora and insect remains (Schneider et al., 2005) and is further constrained by a U-Pb sensitive high-resolution ion microprobe (SHRIMP) zircon age from a tuff in the upper part of the overlying Siebigerode Formation (Wettin Subformation; 299.0 ± 3.2 Ma [2 s], reported in Schneider & Scholze, 2018).

The sample selected for U-Pb LA-ICP-MS carbonate dating comes from a gray limestone domain that is composed of micritic material with biota replaced by white or transparent spar and by an irregular layer of bioclasts that are cemented by brown or transparent spar. The bioclasts are represented by characean algae fragments with carbonate encrustations. The carbonate crusts and micrite have locally entrained fine-grained clastic particles.

The third sample (DH-1) is an orthide brachiopod (*Cyrtonotella semicircularis*, Eichwald, 1829) from the Popovka River section, near Pavlovsk, Saint Petersburg Region, Russia. Both valves of the specimen are preserved within a matrix of micritic limestone that contains abundant fine-grained detrital material. The stratigraphic range of the species is the Aseri Regional Stage (Hints, 2014) according to the Baltoscandian regional chronostratigraphy (c. 465.2 to 463.2 Ma, Lindskog et al., 2017).

2.2. Analytical Methods

Experiments were performed on a Photon Machines Analyte Excite 193 nm ArF excimer laser ablation system coupled to an Agilent 7900 quadrupole ICP-MS (Q-ICP-MS) at the Geology Department of Trinity College Dublin (see Table 1 for operating conditions). Coupling of the Helex 2-volume ablation cell and ICP-MS instrument was realized using either conventional 2 mm inner diameter Teflon tubing or an Aerosol Rapid Introduction System (ARIS; Teledyne Photon Machines). The latter is designed to allow for combined wash-in and wash-out times of down to <20 ms to baseline due to minimal transfer volume and turbulence and is particularly beneficial for the acquisition of highly time-resolved data (van Malderen et al., 2016).

Samples were ablated along linear scans ("rasters") of usually 5 to 20 mm length typically corresponding to ~2 to 8 min of data acquisition per line. Linear scans are arranged in successive order, with no overlaps or gaps between line scans. The required number of rasters making up the final map is dictated by specific features of each sample, such as the presence of clastic contamination or different generations of carbonate, the variation in U/Pb ratio, and on the U concentration. After cleaning with ethanol and then deionized water in an ultrasonic bath a pre-ablation step was used to further remove any surface contamination on the sample. Linear rasters were then undertaken using a fluence of typically 2.5 J/cm^2, high repetition rates of 35 to 40 Hz, square spot dimensions of 47 to 95 μm and continuous stage movement rates of 20 to 40 μm/s under the fixed ablation site (Table 2).

The sample aerosol is transported by He carrier gas, and prior to entering the torch it is mixed with Ar carrier gas from the ICP-MS and with a small amount of N_2 to enhance sensitivity and reduce oxide formation (Hu et al., 2008; Table 1). Daily optimization of the ICP-MS was undertaken using rasters on National Institute of Standards and Technology (NIST) 612 reference glass to yield maximum sensitivity for high masses, Th/U

Table 2
Operational Settings and Map Resolution

Sample	Spot size (μm)	Scan speed (μm/s)	Mass sweep (ms)	Averaged mass sweeps	Effective mass sweep (ms)	Resolution pixel height × width (μm)	Number of linear rasters	Dimension of map (mm width × mm height)
JS4	80	40	139	5	695	80 × 27.8	25	4.8 × 2.0
DBT64-2	80	40	139	5	695	80 × 27.8	20	2.0 × 1.6
JS4b	47	40	134.5	4	538	47 × 21.5	20	5.0 × 1.0
DBT64-1	80	30	139	4	556	80 × 16.7	15	3.6 × 1.2
DH-1	95	20	179.5	5	898	95 × 18.0	10	6.0 × 0.95

ratios of unity as well as low production rates of oxides (ThO^+/Th^+ typically <0.1%) and doubly charged ions ($^{44}Ca^{++}/^{44}Ca^+$ usually <0.35%). Gas flows as well as the sampling depth (torch Z-position) and radio frequency power were kept constant. Dwell times for major and trace elements (^{24}Mg, ^{43}Ca, ^{55}Mn, ^{57}Fe, ^{71}Ga, ^{85}Rb, ^{88}Sr, ^{90}Zr, ^{137}Ba, and ^{140}Ce) are short (typically 2.5 ms, except for 5 ms for ^{43}Ca), while those for Th, Pb, and U isotopes allow for somewhat longer data acquisition (typically ^{204}Pb: 5 to 15 ms, ^{206}Pb: 15 to 40 ms, ^{207}Pb: 20 to 50 ms, ^{208}Pb: 2.5 to 7.5 ms, ^{232}Th: 5 ms, ^{238}U: 15 to 20 ms). Total mass sweep times (including settling times) are typically around 135 to 180 ms (Table 2).

Analyses of the calcite standard WC-1 and synthetic glass NIST 614 reference materials were used to bracket analyses of unknowns. The WC-1 carbonate standard is a marine calcite cement that filled a fault-related discordant Neptunian dyke in the Permian Reef Complex of the Delaware Basin of West Texas. It yields an age of 254.4 Ma, has an average U concentration of approximately 5 ppm, and contains high but variable (85% to 98%) proportions of radiogenic lead (Roberts et al., 2017). Regardless of the type of material analyzed (reference materials or unknowns) a washout of 25 s was allowed between rasters to avoid carry-over from one analysis to the next. The latter part of the signal acquired during washout periods was used for the baseline determination.

2.3. Monitored Masses

Carbonate rocks and minerals form in diverse geological environments under varying conditions and are prone to postformational recrystallization and alteration processes that may result in (local) open system behavior of the U-Pb system and/or in the formation of different generations of carbonate minerals. Extraction of age information from such materials is often difficult or impossible. However, mapping the chemical composition of a sample and relating its geochemistry to textural and/or structural features may assist in discriminating between different age and/or alteration domains in a sample. To this end, a number of elements are monitored in the U-Pb image mapping approach to assist in the interpretation of the U-Pb isotope data. This list of monitor elements can be adjusted depending on the paragenesis of the analyzed samples.

The most common carbonate minerals of the trigonal calcite and dolomite groups (and their major cations) include calcite (Ca), siderite (Fe), magnesite (Mg), dolomite (CaMg), ankerite (Ca [Fe,Mg,Mn]), and kutnohorite (CaMn). The orthorhombic crystal system of the aragonite group minerals allows for the substitution of the larger cations Sr, Ba, and Pb. Monitoring these elements in combination with trace elements facilitates characterization of variations in mineralogy and may also yield evidence for previous mineral transformations (e.g., dolomitization of aragonite, dedolomitization). To characterize the extent of detrital input (typically fine-grained clays and micas) during deposition of sedimentary carbonates, the trace elements Ga, Rb, Zr, and Th serve as reliable proxies as they are enriched in clay minerals/micas and/or are sorbed to clay particles. Detrital U-bearing accessory minerals such as zircon, titanite, monazite, or apatite are also visible on image maps as discrete zones of enrichment of Zr, Ce, Th, and/or U. Finally, migration and redistribution of elements during diagenesis and postformational fluid activity may be indicated by the spatial patterns of elements such as Mg, Mn, Fe, Sr, and U (e.g., Brand & Veizer, 1980; Flügel, 2010; Reinhold, 1998).

Initial homogeneity of the Pb isotope composition and a closed U-Pb system are the key requirements for an isochron-based derivation of a U-Pb age. Therefore, the identification and separation of genetically unrelated components (i.e., input of detrital material) or domains with potentially different initial Pb composition and/or different ages of isotopic closure (e.g., younger generations of diagenetic carbonate) is essential for the derivation of a meaningful U-Pb date and its interpretation.

3. Data Processing

3.1. Initial Data Treatment

One mass sweep (including settling times) typically comprises ~135 to 180 ms depending on the suite of elements used for monitoring the presence of detrital contamination or different generations of carbonate. For a laser scan speed of 40 μm/s, the ablation site will have moved by ~5.56 μm between the first and the last mass measured during one mass sweep. As the washout times are rapid, this means that the sampled volume is not exactly the same for each mass, which may be problematic if the sample is heterogeneous on the scale of the laser spot size or smaller. To reduce the effect of sequential sampling of the individual masses within the same mass sweep, we average over four to five mass sweeps. This also reduces the effect of multiplicative

noise (flicker; from the ICP and LA system) on the isotopic ratios and results in effective mass sweeps or acquisition times per pixel of ~560 to 900 ms.

3.2. Data Processing in Iolite

The data are processed in Iolite (Paton et al., 2010, 2011) using the Trace_Elements and the VisualAge_UcomPbine data reduction schemes (DRS; Chew et al., 2014; Petrus & Kamber, 2012), to undertake baseline and drift corrections and normalization to a primary standard material. NIST 614 standard glass is used as the primary reference material for calibration of both the elemental concentration data and the U-Pb isotope data. Normalization values for NIST 614 are those recommended by Jochum et al. (2011) for the elemental concentrations, the Pb isotopic ratios of Woodhead and Hergt (2001), and a $^{206}Pb/^{238}U$ isotopic ratio of 0.81084 calculated from those values and the U isotopic composition determined by Duffin et al. (2015). Importantly, the Pb isotopic composition of NIST 614 is accurately and precisely know from ID thermal ionization mass spectrometry (ID-TIMS) analyses (Woodhead & Hergt, 2001); the NIST 614 U-Pb ratio is used to calculate a U/Pb fractionation factor between NIST 614 and the analyzed carbonates. Hence, the absolute NIST 614 U/Pb value is not important; all NIST 614 analyses were undertaken on small portions near the wafer center to avoid any potential U/Pb heterogeneity in the reference material (cf. Eggins & Shelley, 2002).

Element distribution maps are constructed from the results obtained from the Trace_Elements DRS using a semiquantitative standardization method (i.e., normalization relative to NIST glass with no internal isotope standard). Isotope maps for the U-Pb data are created from the results obtained from the VisualAge_UcomPbine DRS. As we are using shallow rasters, laser-induced U/Pb fractionation is significantly reduced (cf. Košler & Sylvester, 2003), and accordingly the down-hole fractionation is modeled in Iolite using a linear correction ($y = a + bx$) with zero slope ($b = 0$). Employing the VisualAge_UcomPbine DRS (but with no common Pb correction applied to the NIST 614 primary standard) has the advantage that a common lead-corrected age of the carbonate standard WC-1 can be calculated directly in Iolite. This allows straightforward assessment of the within-run reproducibility of the U-Pb data of the carbonate reference material and provides an estimate of the U/Pb fractionation factor between the primary reference material NIST 614 (a silicate glass) and the carbonate secondary standard (and hence also the carbonate unknowns). Final concentration data were determined using the Trace_Elements DRS by normalizing relative to NIST glass using an internal standard element. All samples in this study are low-Mg calcite, and hence Ca was assumed stoichiometric and used as an internal standard element. Final concentration data and U-Pb isotopic data are reported in supporting information Data Set S1.

3.3. Subsequent Data Processing Using Monocle

The Iolite-processed data are then loaded into the Monocle add-on for Iolite (Petrus et al., 2017), a flexible interrogation tool which enables extraction of data from regions of interest on 2-D elemental and isotope maps. Monocle can construct maps from all available data channels, which in this study comprises all channels generated by the Trace_Elements and the VisualAge_UcomPbine DRS. Monocle also facilitates the construction of additional (elemental or isotopic ratio) maps from all individual data channels. For U-Pb carbonate dating, element ratio maps such as Mg/Ca, Mg/Fe, or Ca/Sr are very useful for assessing spatial variation in chemistry or mineralogy, while isotope ratio maps such as $^{238}U/^{208}Pb$ are used to evaluate the spread in U/common Pb ratios in low-Th samples. The Monocle approach to U-Pb data processing adopted here is based on the selection and pooling of pixels from a 2-D map according to certain criteria, and a worked example is described later and illustrated in Figure 1. Portions of the sample with elevated detrital components, alteration zones, or chemically different generations of carbonate minerals can be identified and rejected by defining appropriate selection criteria (e.g., Rb $<$ 0.5 ppm; Th $<$ 0.5 ppm; Mg/Ca $<$ 0.004). The pixels which pass the selection filter are then pooled into a set of U-Pb analyses. For example, a map may be composed of 5,000 pixels (i.e., 5,000 effective mass sweeps), of which 40% (2,000 pixels) pass the user-defined selection criteria. The pooling of these 2,000 pixels is based on an empirical cumulative distribution function (ECDF) of an element or isotopic ratio, with the goal of obtaining the largest possible spread in U-Pb data on a concordia or isochron diagram. The user chooses the number of ECDF "steps" which corresponds to the total number of analyses on a concordia or isochron; in the example above if 40 U-Pb analyses are desired, each analysis (=ECDF step) will comprise 50 pixels.

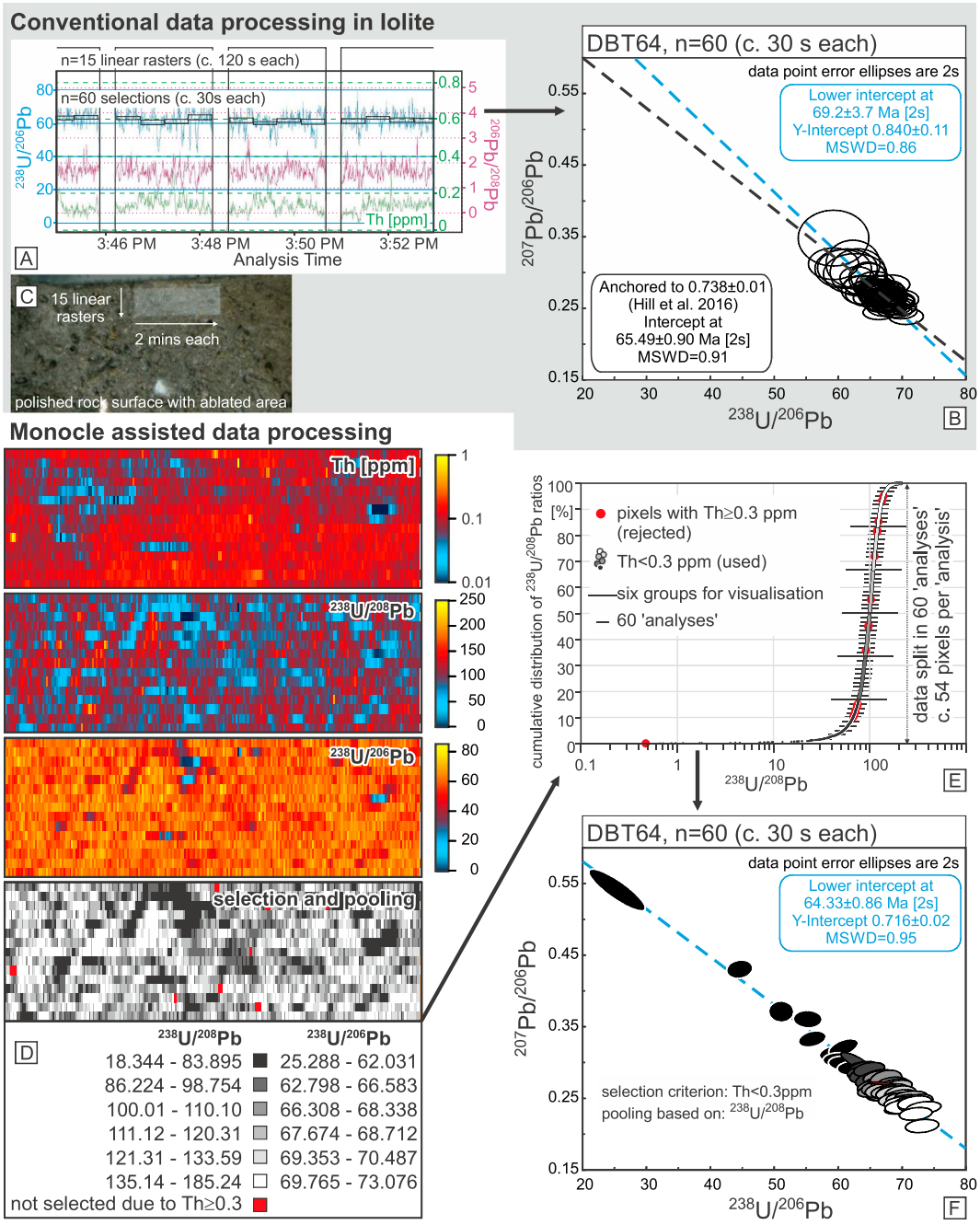

Figure 1. Analysis of the Long Point limestone from Duff Brown Tank locality (DBT64-1). All panels employ the same raw data set. (a) Conventional data processing in lolite by manual selection of adjacent data points of the time-resolved signal and (b) Tera-Wasserburg concordia of these selections. (c) The linear rasters on the polished surface of the sample corresponding to an area ~3.6 mm by 1.2 mm. (d) Selected element and isotope ratio maps created by Monocle. The selection of pixels was based on the Th concentration and resulted in rejection of 16 pixels with Th ≥ 0.3 ppm. Pooling of the remaining 3,245 pixels into 60 "analyses" was based on the $^{238}U/^{208}Pb$ ratio. (e) Cumulative distribution plot illustrating the range and distribution of the $^{238}U/^{208}Pb$ ratios in the mapped area (gray scale as in d). Splitting the data into 60 analyses led to pooling of ~30 s worth of signal. (f) Tera-Wasserburg concordia of the pooled empirical cumulative distribution function "steps" based on their $^{238}U/^{208}Pb$ ratios (gray scale as in d). The pooling results in a larger spread on the U-Pb data points and therefore better accuracy and precision on the U-Pb age.

U-Pb LA-Q-ICP-MS carbonate data are typically plotted on Tera-Wasserburg concordia ($^{207}Pb/^{206}Pb$ vs. $^{238}U/^{206}Pb$), and choosing either of these two isotopic ratios as the ECDF pooling criterion would clearly maximize the U-Pb data spread on Tera-Wasserburg concordia. However, a quadrupole ICP-MS analyses masses sequentially, and so when sampling an inherently noisy and highly transient laser-ablation signal, there is a larger amplitude in the time-resolved isotopic-ratio signal compared to a system equipped with a simultaneous detector such as a MC-ICP-MS where temporal variations in flicker noise do not influence the isotopic-ratio signal. Choosing an ECDF pooling criterion based on (e.g.) the $^{238}U/^{206}Pb$ ratio can result in artifacts on isochron diagrams, as the ECDF steps corresponding to the low and high portions of the $^{238}U/^{206}Pb$ signal are dominated by transient spikes on this isotopic ratio.

To avoid such artifacts, another isotopic ratio which still results in a large spread in U/Pb on Tera-Wasserburg concordia is required. Employing ^{204}Pb to yield a large spread in U/common Pb ratios (e.g., $^{238}U/^{204}Pb$) is hindered by the low isotopic abundance of ^{204}Pb and by isobaric interference of ^{204}Hg on ^{204}Pb, which cannot be sufficiently corrected for in LA-Q-ICP-MS analyses without prohibitively long dwell times on ^{202}Hg and $^{204}(Pb + Hg)$. Based on these constraints, our experiments show that the $^{207}Pb/^{235}U$ ratio (for pre-Cenozoic samples) or the $^{238}U/^{208}Pb$ ratio (for low Th samples) appears to be most suitable ratio for pooling the data into discrete ECDF steps. Whether the $^{207}Pb/^{235}U$ or the $^{238}U/^{208}Pb$ ratio is employed depends on the age and the U, Th, and Pb concentrations of the sample. The number of analyses (=ECDF steps) is user-defined and depends on the number of pixels which pass the selection criteria, the cumulative distribution of values in the pooling channel, and the concentrations of U, Th, and Pb (counting statistics). For example, ~30 s of signal per ECDF step, which would be similar to the typical analysis time of a LA-ICP-MS spot analysis, would comprise 43 pixels (five mass sweeps of 140 ms averaged to give 700 ms of analysis time per pixel). A considerable increase in the number of pixels pooled in one analysis can be beneficial for low U ($<$0.5 ppm) or young (Cenozoic) samples with poor counting statistics on U and/or radiogenic Pb.

3.4. Final Processing in MS Excel

The Monocle-processed data were loaded into an MS Excel spreadsheet with the Isoplot add-on (Isoplot 4.15; Ludwig, 2012). In this last step, a matrix-dependent U-Pb fractionation correction is applied to the unknowns if necessary. An anchored (initial $^{207}Pb/^{206}Pb$ 0.85 ± 0.04, Roberts et al., 2017) linear regression of the NIST 614-normalized WC-1 carbonate data is used to obtain a lower intercept age on Tera-Wasserburg concordia. A U-Pb fractionation factor is then applied to the WC-1 carbonate $^{206}Pb/^{238}U$ (and $^{207}Pb/^{235}U$) ratios such that the WC-1 carbonate age yields its accepted value of 254.4 Ma (Roberts et al., 2017). The WC-1 carbonate U/Pb data usually show an excess variance of around 1.5% to 3% per session, which is propagated through to the $^{238}U/^{206}Pb$ ratio of the unknowns. For the Pb/Pb ratios the uncertainty on the NIST glass $^{207}Pb/^{206}Pb$ and $^{208}Pb/^{206}Pb$ ratios (typically ~0.3% to 0.9%) is propagated through to the unknowns.

A linear regression of the ECDF data in Tera-Wasserburg space is then undertaken to obtain the initial $^{207}Pb/^{206}Pb$ ratio, the lower intercept date, and their associated uncertainties and statistics using Isoplot. To test for consistency of the data, two additional dates are calculated from the same data set: an isochron age from $^{206}Pb_{total}/^{208}Pb_{common}$ versus $^{238}U/^{208}Pb_{common}$ (e.g., Getty et al., 2001) and the 86TW age (*sensu* Parrish et al., 2018) employing $^{208}Pb_{common}/^{206}Pb_{total}$ versus $^{238}U/^{206}Pb_{total}$. These two additional approaches to age calculation require correction for radiogenic ^{208}Pb ingrowth in Th-bearing samples.

All U-Pb data including the calculated intercept and isochron dates are reported in supporting information Data Set S1. Uncertainties on the U-Pb dates and initial $^{207}Pb/^{206}Pb$ ratios are given at the 2 s or 95% confidence level, respectively, throughout this paper.

4. Results

4.1. The Monocle Approach—Example 1 (Sample DBT64-1): Improving the Spread in Parent/Daughter Ratios

Figure 1 illustrates the problem of data points with an insufficient spread in parent/daughter ratio, using sample DBT64 (the Long Point limestone sample from the Duff Brown Tank locality). To construct the initial Tera-Wasserburg plot in Figure 1b, we used 60 successive manual selections (each comprising ~30 s of data acquisition) from 15 linear rasters each representing ~120 s of data acquisition (Figures 1a and 1c). The data were processed in Iolite using the VisualAge_UcomPbine DRS, and the $^{238}U/^{206}Pb$ ratios were subsequently

corrected by the matrix-dependent fractionation factor. The limited spread in $^{238}U/^{206}Pb$ ratios (59.224 to 70.630) results in an imprecise $^{207}Pb/^{206}Pb$ intercept of 0.840 ± 0.110 and in an imprecise and inaccurate lower intercept date of 69.2 ± 3.7 Ma (Figure 1b) (cf. reported values: initial $^{207}Pb/^{206}Pb$ = 0.738 ± 0.01, age = 64.04 ± 0.67 Ma; Hill et al., 2016). Anchoring the regression line to the initial Pb composition reported by Hill et al. (2016) yields a more precise lower intercept date of 65.5 ± 0.9 Ma (Figure 1b). However, for most unknowns the initial $^{207}Pb/^{206}Pb$ composition is not known independently but only as a result of a linear regression from the same data set and hence cannot be used as an initial $^{207}Pb/^{206}Pb$ constraint on a Tera-Wasserburg isochron or ^{207}Pb-corrected age. Therefore, selection and pooling of data with Monocle is a valuable tool for most data sets to retrieve the largest possible spread in $^{238}U/^{206}Pb$ ratios and thus the best possible precision on both the $^{207}Pb/^{206}Pb$ initial ratio and the $^{238}U/^{206}Pb$ lower intercept age, respectively.

To demonstrate this, Figure 1f presents a Tera-Wasserburg plot of the same raw data set as shown in Figure 1 b. The 15 linear rasters were again processed with Iolite, but instead of making manual selections from the time-resolved signal, the processed data were loaded into Monocle (Petrus et al., 2017) to make 2-D elemental and isotopic maps. Monocle creates a separate map for each Iolite output channel with each pixel corresponding to one time slice; some of these maps are shown in Figure 1d. The data set was then filtered by only selecting pixels with a Th content of $<$0.3 ppm. The Th concentration is very low throughout the sample, and only 16 of 3,261 pixels were rejected (i.e., Th $\geq$ 0.3 ppm). The 3,245 selected pixels were then pooled into 60 analyses using an ECDF on the $^{238}U/^{208}Pb$ ratio (Figure 1e), as the $^{238}U/^{208}Pb$ ratio monitors both the abundance of the parent isotope (^{238}U) and the proportion of common Pb (^{208}Pb) in this low Th Cenozoic sample. A total of 60 analyses was chosen to yield ~30 s of signal per analysis which is comparable with (i) the Tera-Wasserburg plot in Figure 1b constructed from manual selections of the time-resolved signal and (ii) spot ablation data from the literature which are typically acquired for ~20 to 30 s (e.g., Burisch et al., 2017; Coogan et al., 2016; Nuriel et al., 2017; Ring & Gerdes, 2016; Roberts & Walker, 2016). Compared to the data processed by manual selections in Iolite, the Monocle approach yields a better precision for the individual analyses as well as a larger spread in $^{238}U/^{206}Pb$ ratios (25.288 to 73.076) and therefore a better precision on both the $^{207}Pb/^{206}Pb$ initial ratio and the $^{238}U/^{206}Pb$ lower intercept age. The lower intercept age of 64.33 ± 0.86 Ma and $^{207}Pb/^{206}Pb$ initial ratio of 0.716 ± 0.016 are within uncertainty of the previously reported values (Hill et al., 2016). Importantly, the precision of the Hill et al. (2016) age (64.04 ± 0.67 Ma), which was obtained using a significantly more time-intensive ID approach with a more precise instrument (MC-ICP-MS), is only moderately better than that of our age determination (± 0.86 Ma).

4.2. The Monocle Approach—Example 2 (Sample JS4, Run JS4-1): Selection of Pixels in Texturally and Chemically Complex Carbonate Rocks

Another example of the use of Monocle for the extraction of U-Pb carbonate age data is based on the analysis of the Carboniferous-Permian lacustrine limestone sample JS4. This sample consists of texturally variable domains comprising micritic material, uncompacted encrusted bioclasts, and yellow transparent spar filling in the pore space between encrusted bioclasts. Figure 2a shows several element, element ratio, and isotope ratio maps constructed using Monocle from the semiquantitative trace element analyses and the U-Pb data. Differences in elemental and isotopic composition clearly correspond to petrographic and textural features. The micritic material shows the highest concentrations in Mg, Th (Figure 2a), Sr, and Ba (not shown in figure) while the micrite and encrusted bioclasts display similarly high contents in Fe, Rb (Figure 2a), Zr, and Ce (not shown in figure). In contrast, the spar overgrowing the encrusted bioclasts is enriched in Mn compared to the micrite and bioclasts and is depleted in nearly all other monitored elements. The U concentration in the spar shows a gradient from rim ($\geq$15 ppm U) to center ($\leq$1 ppm) and, therefore, controls the parent/daughter ratio and the data spread in Tera-Wasserburg space.

From textural relationships the spar was the latest phase to be precipitated in this sample, and both microscopic observations and image maps of the spar did not reveal indications of a detrital component or of post-formational fluid ingress (Figure 2a). Using the criterion Th $<$ 0.5 ppm to select the pixels corresponding to the late spar (Figures 2d and 2e) and employing the $^{207}Pb/^{235}U$ channel for splitting and pooling of the pixels into analyses gives a lower intercept date of 297.8 ± 3.3 Ma and an initial $^{207}Pb/^{206}Pb$ value of 0.857 ± 0.002 (Figure 2b) when combining ~30 s of signal per analysis and regressing the 38 data points on a Tera-Wasserburg plot. A $^{206}Pb/^{208}Pb_{common}$ versus $^{238}U/^{208}Pb_{common}$ isochron plot (297.2 ± 3.9 Ma) and a $^{208}Pb_{common}/^{206}Pb_{total}$ versus $^{238}U/^{206}Pb_{total}$ regression (297.0 ± 2.9 Ma) of the same data set yield similar

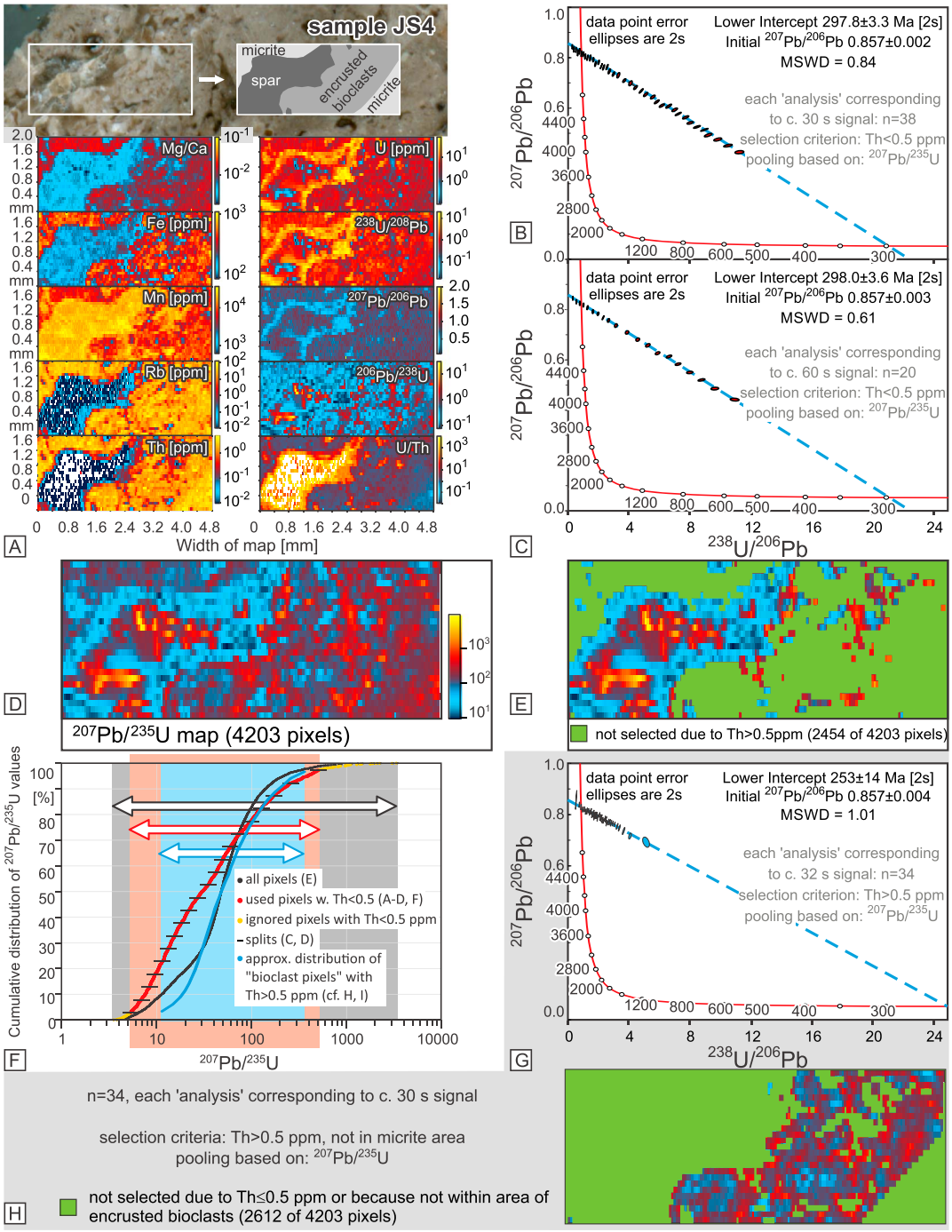

Figure 2. Analysis of Carboniferous-Permian lacustrine limestone sample JS4 (run JS4-1). (a) The polished rock slab of the sample with an outline of the mapped area and the major textural domains are shown in the top panel. The element, elemental ratio, and isotope ratio maps below were constructed by Monocle from 25 linear rasters and correspond to an area of 4.8 mm by 2.0 mm. (b, c) Tera-Wasserburg concordias for the transparent spar in sample JS4. (d) $^{207}Pb/^{235}U$ map of all 4,203 pixels. (e) Pixels used for construction of the Tera-Wasserburg diagrams in b and c after rejection of 2,454 pixels corresponding to a Th content ≥0.5 ppm. (f) Cumulative distribution plot of the $^{207}Pb/^{235}U$ ratios for different domains of the sample (black curve = all pixels; red curve = pixels corresponding to Th < 0.5 ppm and corresponding to transparent spar; blue curve = pixels with Th > 0.5 ppm corresponding to encrusted bioclasts). The respective ranges in $^{207}Pb/^{235}U$ are indicated by white arrows and a black, red, or blue outline. Monocle allows cropping of the data set at the lower and upper limits of the cumulative distribution function to avoid the inclusion of spurious data. Such cropping was applied to the data in (b) and (c). The $^{207}Pb/^{235}U$ ratios of these ignored pixels are shown in yellow in the diagram. (g) Tera-Wasserburg concordia derived from pixels corresponding to the encrusted bioclasts and yielding an unreasonably young lower intercept date of 253 ± 14 Ma. (h) Selected pixels in the domain of encrusted bioclasts used in the construction of panel g with a Th content ≥0.5 ppm. The spread in U/Pb ratio is much smaller (see also the light blue shaded area in f) than in the transparent spar (see the light red shaded area in f) and resulting in a poorly constrained lower intercept. See text for further explanation.

U-Pb dates for this low Th, texturally late spar (not shown in figure). Both the initial $^{207}Pb/^{206}Pb$ and $^{206}Pb/^{208}Pb$ values for this sample are within uncertainty of the $^{207}Pb/^{206}Pb$ and $^{206}Pb/^{208}Pb$ values derived from the Stacey and Kramers (1975) terrestrial Pb evolution model at the time (298 Ma) of spar growth (0.8554 and 0.4791 respectively). Pooling the pixels in 20 analyses with ~57 s worth of signal per analysis (instead of the previous 38 analyses of ~30 s each) yields similar results (Tera-Wasserburg lower intercept of 298.0 ± 3.6 Ma with a $^{207}Pb/^{206}Pb_{initial}$ of 0.857 ± 0.003 [Figure 2c]; $^{206}Pb/^{208}Pb_{common}$ versus $^{238}U/^{208}Pb_{common}$ isochron date of 298.1 ± 4.5 Ma with a $^{206}Pb/^{208}Pb_{initial}$ of 0.4779 ± 0.002 and 86-TW intercept of 297.8 ± 3.5 Ma with $^{208}Pb/^{206}Pb_{initial}$ of 2.092 ± 0.007 [not shown in figure]).

The pooling of the data set into analyses (=ECDF steps) for different textural domains is illustrated in Figure 2f. For the transparent spar (Th $<$ 0.5 ppm) the $^{207}Pb/^{235}U$ ratios span 2 orders of magnitude (5.190 to 512.95), and their cumulative distribution curve has a relatively uniform and gentle slope over this range (red curve in Figure 2f). Importantly, there are data with relatively low $^{207}Pb/^{235}U$ (i.e., a high parent/daughter ratio) which result in data points closer to the lower intercept in Tera-Wasserburg space (Figures 2b and 2c), which is key for a well-constrained lower intercept age.

In contrast, $^{207}Pb/^{235}U$ ratios corresponding to the domain of encrusted bioclasts (the pixels selected using the criterion Th $>$ 0.5 ppm and avoiding the micritic area by applying the selection criterion to a manually drawn region of interest; Figure 2h) have a cumulative distribution that spans only little more than 1 order of magnitude ($^{207}Pb/^{235}U$ ratios from 11.03 to 364.88; blue curve in Figure 2f). Data points plot much closer to the $^{207}Pb/^{206}Pb$ axis and result in a rather poorly constrained lower intercept of 253 ± 14 Ma (Figure 2g). This U-Pb date for the encrusted bioclasts is considerably younger than the U-Pb date of the texturally later spar.

The pixel selection criterion of Th $<$ 0.5 ppm for the domain of transparent spar does not eliminate all time slices which potentially include detrital material as analyses still yield elevated ($>$0.5 ppm) Rb and Zr concentrations. Using more conservative selection criteria (pixels with all of Rb, Zr, and Th $<$ 0.3 ppm) and employing the $^{207}Pb/^{235}U$ channel for splitting and pooling of the pixels into analyses yields a lower intercept date of 300.8 ± 3.7 Ma and an initial $^{207}Pb/^{206}Pb$ value of 0.858 ± 0.003 (Figure 3a) with each analysis representing ~30 s of signal and regressing the data points in a Tera-Wasserburg plot. A 86-TW plot of the same data set yields a similar date of 299.6 ± 4 Ma and an initial $^{208}Pb/^{206}Pb$ value of 2.090 ± 0.008 (Figure 3b) for this low Th, transparent spar domain. Again, both the initial $^{207}Pb/^{206}Pb$ and $^{206}Pb/^{208}Pb$ values determined from the sample are within uncertainty of the $^{207}Pb/^{206}Pb$ and $^{206}Pb/^{208}Pb$ values calculated from the Stacey and Kramers (1975) model at the time of spar formation (0.8554 and 0.4791, respectively).

Figures 3e and 3f show Tera-Wasserburg concordia diagrams for the entire data set obtained from lacustrine limestone sample JS4, with no exclusion of any pixels. The data set was pooled into 91 analyses (~32 s each) again using the $^{207}Pb/^{235}U$ ratio. Interestingly the lower intercept date of 299.6 ± 3.7 Ma is identical within analytical uncertainty to the lower intercept date obtained from the cleanest spar domain (cf. Figures 3a and 3b), but the calculated $^{207}Pb/^{206}Pb$ initial ratio of 0.866 ± 0.002 is elevated (cf. 0.858 ± 0.003 for clean spar, Figure 3a, and 0.858 ± 0.004 for encrusted bioclasts, Figure 2g) and the arrangement of the error ellipses along the regression line is nonlinear (Figures 3e and 3f). The 15 ellipses with the highest proportions of radiogenic Pb (29% to 60%; shown in green in Figures 3e and 3f) largely correspond to the transparent spar (cf. green area in map inset in Figure 3f) and control the lower intercept with the concordia curve. Analyses with higher proportions of initial Pb represent varying admixtures of pixels from encrusted bioclasts and transparent spar. These data points fall along an array between the discordia line for the transparent spar and that of the encrusted bioclasts (Figures 3e and 3f) and skew the data point regression toward an unreasonably high $^{207}Pb/^{206}Pb$ initial ratio.

4.3. The Monocle Approach—Example 3 (Sample DH1): Selection of Pixels in Texturally and Chemically Complex Biogenic Calcite

A sample of a fossil brachiopod shell (sample DH-1) is used to demonstrate the application of the image mapping technique to biogenic low-Mg calcite. The shell was sampled from a micritic limestone, and both valves of the brachiopod are preserved and enclose an infilling of micritic carbonate. Figure 4a shows a polished section of the specimen embedded in epoxy. Both SEM imaging and LA-ICP-MS image mapping (Figures 4b and 4c) reflect the microstructure of the shell (Figure 4a-2) comprising the (initially) noncalcareous periostracum

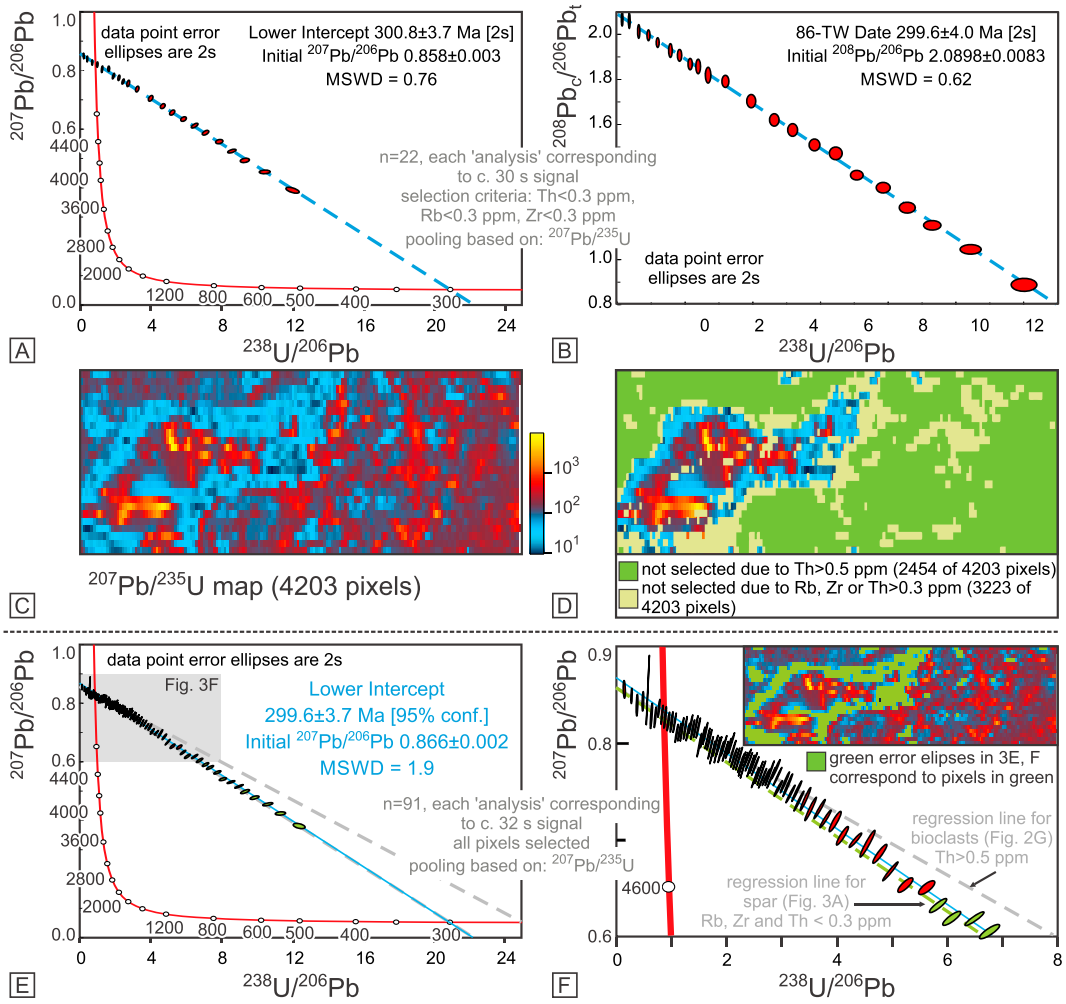

Figure 3. Analysis of Carboniferous-Permian lacustrine limestone sample JS4 (run JS4-1). (a) Tera-Wasserburg concordia and (b) $^{206}Pb/^{208}Pb_{common}$ versus $^{238}U/^{208}Pb_{common}$ isochron plot for the lacustrine limestone sample JS4-1 using the same data set as Figure 2. (c) $^{207}Pb/^{235}U$ map of all 4,203 pixels. (d) Rejected pixels with Th $\geq$ 0.5 ppm (green, 2,454 pixels) and Rb, Zr, and/or Th $>$ 0.3 ppm (green and light green; 3,223 pixels); the remaining 980 pixels correspond to transparent spar devoid of detrital material and were used in the construction of panels a and b. (e, f) Tera-Wasserburg concordia for the entire data set obtained on lacustrine limestone sample JS4 without exclusion of pixels. Regression lines for the data corresponding to the transparent spar (cf. Figure 3a) and to the encrusted bioclasts (cf. Figure 2g) are shown for reference. The 15 ellipses shown in green contain the highest proportions of radiogenic Pb (29% to 60%) and largely correspond to the transparent spar (cf. green area in map inset in Figure 3f). See text for further explanation.

(outermost layer), the primary layer of rather structureless crystalline calcite, and the secondary layer being made up of calcite fibers and inorganic material (innermost layer). The periostracum is depleted in Ca and enriched in many other elements (particularly well visible in the Fe, Rb, Ce, and Th maps in Figure 4c) that are chiefly of detrital and diagenetic origin. The secondary layer also shows elevated concentrations of Mg, Fe, and Ce (Figure 4c) that are indicative of diagenetic modification of the chemical composition. The primary layer appears to be the least altered part of the shell, but element maps (Figure 4c) suggest localized ingress of diagenetic fluids along growth lines (elevated Mg, Fe, Ga, Ce, Pb, and U) within the shell. Selection criteria were chosen to first separate the shell calcite from the surrounding epoxy and periostracum (Ca $>$ 500,000 ppm) and to exclude the altered secondary layer of the shell and adjacent sediment (Rb $<$ 0.1 ppm and Th $<$ 0.1 ppm), which results in 2,490 selected pixels. By employing the $^{207}Pb/^{235}U$ channel for pooling, the data were split into 29 analyses, each of which corresponds to ~60 s of signal. U-Pb dates derived from Tera-Wasserburg regression (470.5 ± 8.4 Ma, Figure 4d), $^{206}Pb/^{208}Pb_{common}$ versus $^{238}U/^{208}Pb_{common}$ isochron (469 ± 11 Ma, not shown), and $^{208}Pb_{common}/^{206}Pb_{total}$ versus $^{238}U/^{206}Pb_{total}$

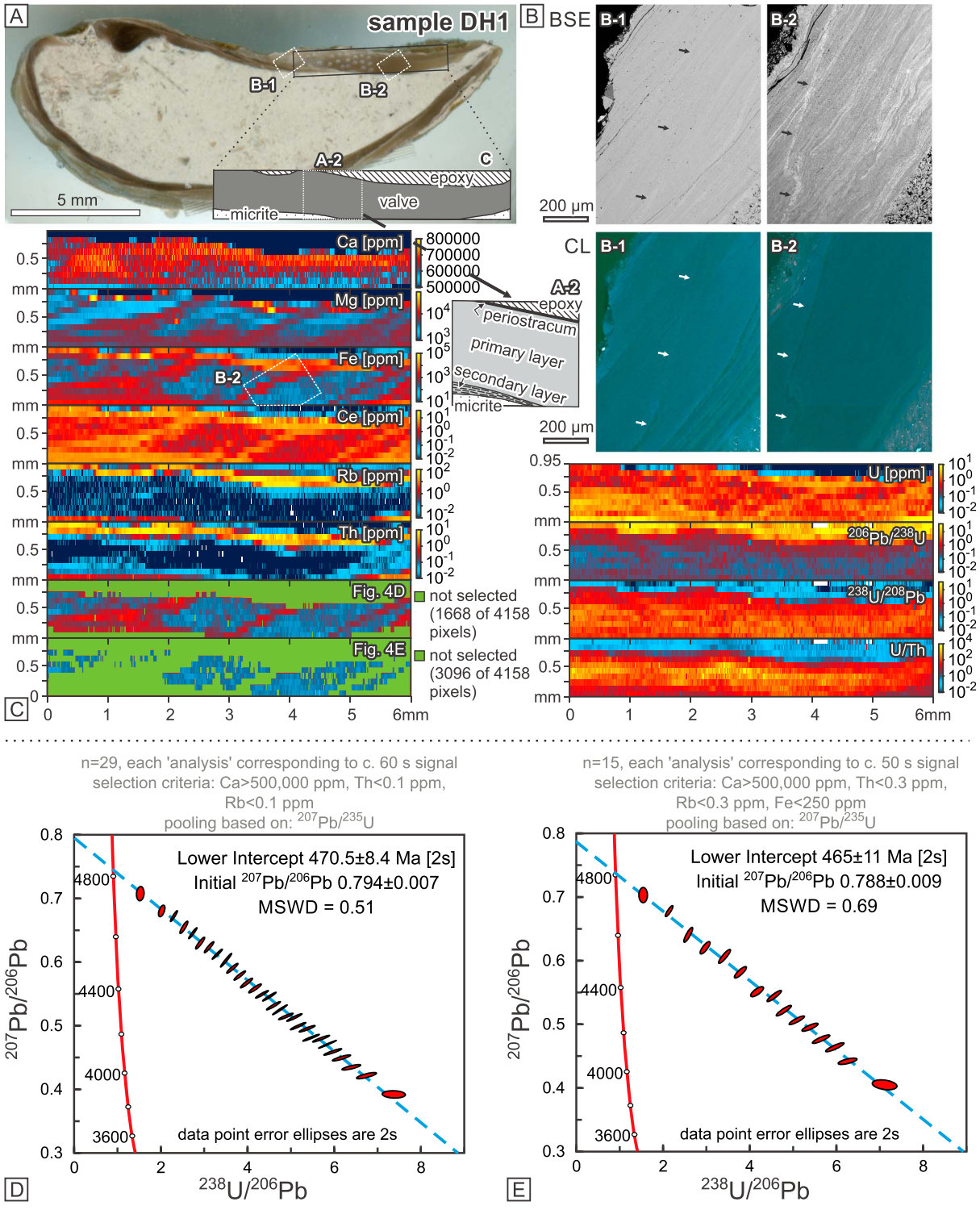

Figure 4. Analysis of brachiopod shell hosted by micritic carbonate sediment (sample DH1). (a) The major textural domains within the sample as well as the location of the backscattered electron (BSE) and cathodoluminescence (CL) images in (b) and the laser ablation maps in (c) are indicated on a scan of the polished section through the shell. The microstructure of the shell is sketched in a-2. (b) Scanning electron microscopy images for two areas in the dorsal valve with the epoxy in the top left corner and the micritic sediment in the bottom right corner. Note the thicker secondary layer in b-1 when compared to the more posterior position in b-2. Arrows indicate growth lines within the primary layer of the shell. (c) The element, elemental ratio, and isotope ratio maps were constructed by Monocle from 10 linear rasters corresponding to a mapped area of 6.0 mm by 0.95 mm. (d) Tera-Wasserburg concordia for 2,490 pixels acquired from the brachiopod shell (sample DH-1). Pixels corresponding to or overlapping the surrounding epoxy and the host sediment were excluded (1,668 pixels). (e) Tera-Wasserburg concordia for 1,062 pixels acquired from the brachiopod shell. In addition to epoxy and detrital material areas with postdepositional overprint (Fe > 250 ppm) were avoided for age calculation (3,096 pixels).

regression (468 ± 9 Ma, not shown) are similar within analytical uncertainty and overlap the expected maximum stratigraphic range (c. 465.2 to 463.2 Ma) of the brachiopod.

Additional exclusion of areas with likely diagenetic overprint (along the growth lines) was accomplished by including the criterion Fe < 250 ppm (Figures 4c and 4e). The selected 1,062 pixels were pooled into 15 analyses (~50 s each) by their $^{207}Pb/^{235}U$ ratios, and the U-Pb dates derived from Tera-Wasserburg regression (465 ± 11 Ma, Figure 4e), $^{206}Pb/^{208}Pb_{common}$ versus $^{238}U/^{208}Pb_{common}$ isochron ($463\ ^{+19}/_{-20}$ Ma, not shown), and $^{208}Pb_{common}/^{206}Pb_{total}$ versus $^{238}U/^{206}Pb_{total}$ regression (466 ± 13 Ma, not shown) are again identical within analytical uncertainty.

The U-Pb dates obtained from these least altered areas of the brachiopod shell are similar within uncertainty with the results achieved by using less conservative selection criteria. They have, however, larger uncertainties due to the considerably reduced number of pixels (1,062 versus 2,490) and a marginally smaller spread in data points along the isochron regression.

5. Discussion

5.1. Accuracy and Reproducibility of the U-Pb Data

To assess the accuracy of the U-Pb carbonate LA-ICP-MS dates, the Long Point limestone sample from the Duff Brown Tank locality (DBT64; Hill et al., 2016) was used as a quality control. This material is run along with the primary (NIST 614 standard glass) and carbonate (WC-1) reference materials and the unknowns and is treated as an unknown during the data reduction. During the analytical session (run JS4-1) in which the texturally complex lacustrine limestone sample JS4 was analyzed, a Tera-Wasserburg lower intercept date of 63.3 ± 1.6 Ma (MSWD = 0.37) was obtained for sample DBT64-2. All pixels yielded Th concentrations <0.3 ppm and Rb concentrations <3 ppm, so no selection criteria were applied in Monocle, and each analysis was constructed by pooling ~60 s of signal using the $^{238}U/^{208}Pb$ ratio. This date is in agreement with the previously established age of 64.04 ± 0.67 Ma (Hill et al., 2016) and suggests that the results of the session are accurate within analytical uncertainty.

Repeat analyses of DBT64 gave dates similar to the previously established age of 64.04 ± 0.67 Ma (Hill et al., 2016) with analytical uncertainties of 0.66 to 1.6 Ma (1.0% to 2.5%), with the magnitude of the analytical uncertainty largely determined by the spread of the data points along the linear regression on Tera-Wasserburg or isochron diagrams, respectively. The uncertainties on the $^{238}U/^{206}Pb$ ratios of the individual analyses were typically around 2.5% to 5.0% for areas with ≥30% radiogenic ^{206}Pb, which is about 1 order of magnitude less precise than the bulk-rock ID analyses of Hill et al. (2016; 0.16% to 0.35% analytical uncertainty on $^{238}U/^{206}Pb$). However, our final lower intercept dates of the regression in Tera-Wasserburg space are only up to 3 times less precise (1.0% to 2.5%) than the ID age (1.1%) and may even reach a precision similar to that of the ID age when the map covers a larger spread in parent/daughter ratios ($^{238}U/^{206}Pb$ 41.951 to 64.332 for ID data of Hill et al., 2016, versus 25.288 to 73.076 for the data in Figure 1f [1.6%]).

During two different sessions a couple of weeks apart we determined two U-Pb dates identical within analytical uncertainty for two separate areas within the transparent spar domain of the lacustrine limestone sample from the Carboniferous-Permian Saale basin. Run 1 of sample JS4 (JS4-1) was discussed earlier, and the data are presented in Figures 2 and 3, while run 2 of sample JS4 (JS4-2) is discussed here and the data are presented in Figure 5. We employed the same selection and pooling criteria for processing both data sets (selection criteria: Rb < 0.3 ppm, Zr < 0.3 ppm, and Th < 0.3 ppm; pooling by $^{207}Pb/^{235}U$). In the second run (JS4-2) the transparent spar domain yields a lower intercept date of 300.5 ± 3.3 Ma (Figure 5c; cf. 300.8 ± 3.7 Ma from the previous run on sample JS4 in Figure 3a) and an initial $^{207}Pb/^{206}Pb$ value of 0.856 ± 0.004 (cf. 0.858 ± 0.003 for JS4-1 in Figure 3a) when employing ~30 s of signal per analysis and regressing the data points on Tera-Wasserburg concordia. A $^{206}Pb/^{208}Pb_{common}$ versus $^{238}U/^{208}Pb$ isochron plot and a $^{208}Pb_{common}/^{206}Pb_{total}$ versus $^{238}U/^{206}Pb_{total}$ regression on the same data set yield similar U-Pb dates of 299.7 ± 5.0 Ma (cf. 298.9 ± 5.6 Ma from the previous run on sample JS4) and 298.8 ± 3.5 Ma (cf. 299.6 ± 4.0 Ma from the previous run on sample JS4). Again, both the initial $^{207}Pb/^{206}Pb$ and $^{206}Pb/^{208}Pb$ values determined from the sample are within uncertainty of the $^{207}Pb/^{206}Pb$ and $^{206}Pb/^{208}Pb$ values calculated from the Stacey and Kramers (1975) model at the time of spar formation (0.8554 and 0.4791,

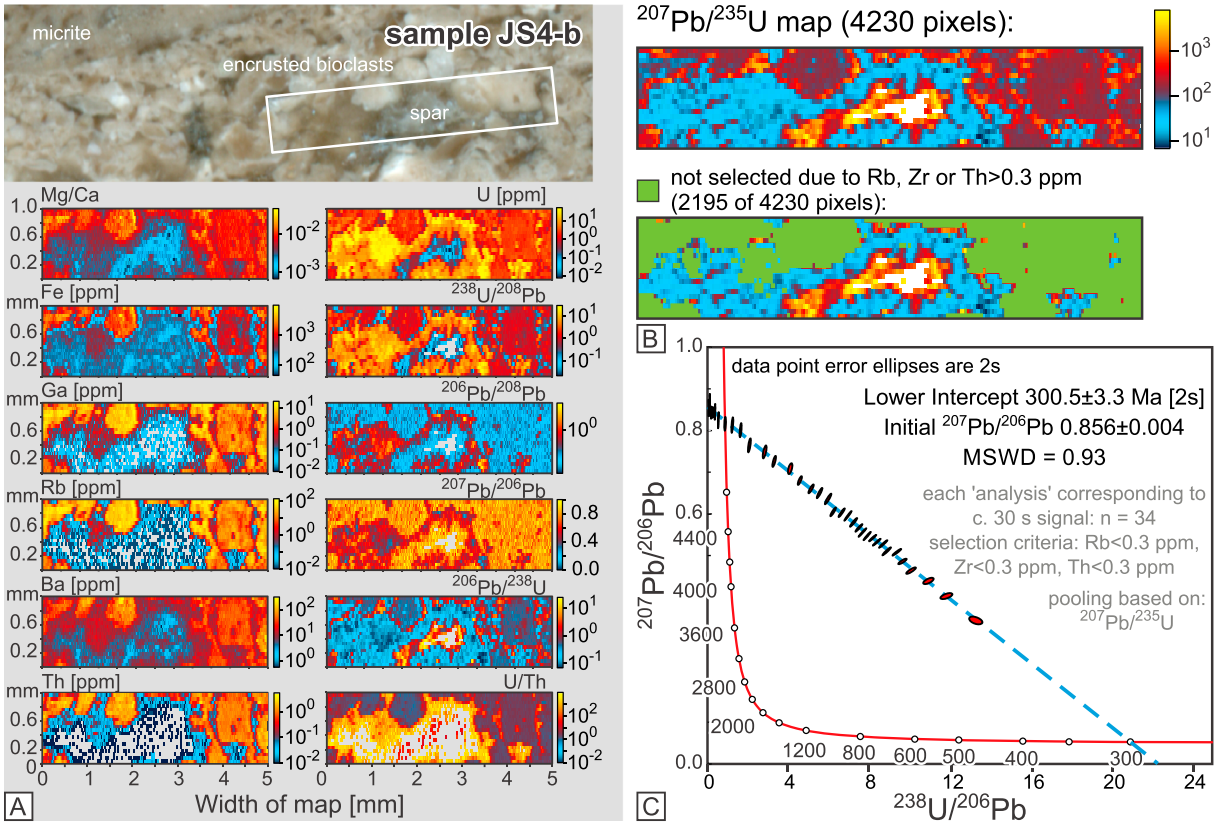

Figure 5. Repeat analysis of Carboniferous-Permian lacustrine limestone sample JS4 (run JS4-2). (a) Scan of a polished rock slab and outline of the mapped area. This is a separate transparent spar domain compared to that mapped in Figures 2 and 3. The element, elemental ratio, and isotope ratio maps below were constructed by Monocle from 20 linear rasters and correspond to an area of 5.0 mm by 1.0 mm. (b) $^{207}Pb/^{235}U$ maps of all 4,230 pixels and showing the pixels rejected due to Rb, Zr, or Th > 0.3 ppm (green; 2,195 pixels). (c) Tera-Wasserburg concordia constructed from U-Pb data of the remaining 2,035 pixels corresponding to transparent spar devoid of detrital material.

respectively). This example shows the excellent reproducibility of the technique and highlights the suitability of criteria-based selections to target the same genetic domain in different areas of the same sample.

5.2. Interpretation of Carbonate U-Pb Age Data

Radiometric dating of carbonates is not just an issue of analytical accuracy and precision. The interpretation of the U-Pb data can also be challenging, as carbonates are prone to subsequent mineral transformations and alteration. All U-Pb data need to be carefully evaluated in combination with independent constraints to establish which event or process is actually being dated. Such information includes stratigraphic and depositional environment constraints, petrography of macroscopic and microscopic textural features, information on the diagenetic or metamorphic history, and elemental and stable isotope geochemical data.

For the complex lacustrine limestone sample JS4, two discrete U-Pb dates were obtained from texturally and chemically different portions of the sample. The texturally older encrusted bioclasts yielded an imprecise U-Pb date of 253 ± 14 Ma clearly postdating deposition of the limestone, while the transparent spar overgrowing these encrusted bioclasts yielded an older U-Pb date of 300.8 ± 3.7 Ma. The encrustations of the bioclasts are characterized by a fine-grained powdery texture with inclusions of detrital material with high Rb, Zr, and Th. Moreover, the data points show little spread on the Tera-Wasserburg diagram and plot close to the *y* intercept (Figure 2g). Although this makes the apparent young age of the encrusted bioclasts difficult to assess, it is most likely that the assumption of a homogeneous initial Pb composition (an essential prerequisite for a successful age determination by the U-Pb method) is not fulfilled in this case. Textural and elemental composition information strongly suggest a mixed/heterogeneous initial Pb composition (differing Pb isotopic compositions in detrital components plus an additional authigenic Pb component) in the encrusted

bioclasts and imply that this portion of the sample is not suitable for direct dating of carbonate sedimentation by the U-Pb method.

The U-Pb date of the crystalline transparent spar (300.8 ± 3.7 Ma) is interpreted as the formation age of the spar and as a minimum age for the deposition of the lacustrine micritic limestone. Textural relationships (the spar overgrows uncompacted encrusted bioclasts) suggests spar formation occurred within the uncompacted sediment during very early diagenesis, probably within a few hundred thousand years after deposition.

The obtained age for the upper Rothenburg Formation is in agreement with the depositional age constraints for the regional stratigraphy. These include the 299.0 ± 3.2 Ma U-Pb SHRIMP zircon age from a tuff in the upper part of the overlying Siebigerode Formation reported in Schneider and Scholze (2018) and a Stephanian (=Kazimovian to Gzhelian) stratigraphic age based on macroflora and insect remains (Schneider et al., 2005). The latter corresponds to a time interval of 307.0 ± 0.1 to 298.9 ± 0.15 Ma based on the estimated age ranges of the Kazimovian and Gzhelian stages (International Chronostratigraphic Chart, v. 2017/2). The age is also in very good agreement with regional biostratigraphical correlations of the Rothenburg and Siebigerode formations with other continental basins within the European Variscides (e.g., Schneider & Scholze, 2018; Schneider & Werneburg, 2012). The depositional ages of these correlative strata have subsequently been constrained in several basins by high-precision U-Pb chemical abrasion ID-TIMS zircon dating on volcanic and volcaniclastic deposits (Autun basin, France—Pellenard et al., 2017; western and central Bohemian basins, Czech Republic—Opluštil, Schmitz, Cleal, & Martínek, 2016; Boskovice basin, Czech Republic—Opluštil et al., 2017; and Intra-Sudetic basin, Czech Republic—Opluštil, Schmitz, Kachlík, & Štamberg, 2016).

The textural observations described above and the U-Pb date of the transparent spar that is within analytical uncertainty of independent depositional age constraints suggests that our U-Pb LA-ICP-MS date of 300.8 ± 3.7 Ma is a close estimate of the true depositional age of the lacustrine micritic limestone.

For the dorsal valve of an orthide brachiopod we determined a U-Pb date of 465 ± 11 Ma. It was determined on a part of the valve that appeared to be least altered as suggested by minor and trace element compositions and by SEM imaging. The obtained date is in good agreement with the biostratigraphic range of the brachiopod (Aseri on the Baltoscandian scale; c. 465.2 to 463.2 Ma—Lindskog et al., 2017), and we consider this U-Pb date a close age estimate for the brachiopod shell and for deposition of the host sediment. The results furthermore suggest the feasibility of the LA-ICP-MS U-Pb dating technique to dating biogenic carbonate materials, particularly brachiopods which typically grow shells of primary calcite (most mollusk shells are composed mainly of aragonite which is metastable on the Earth's surface and inverts to calcite over geological time). Biogenic carbonate material is frequently subject to U mobility/uptake postmortem, and the result highlights the capability of the image mapping technique to target the most pristine parts of such material.

5.3. Advantages and Limitations of the Approach

After integration and careful evaluation of spatially linked textural, mineralogical, and geochemical features, domains with potentially different growth stages or postdepositional overprinting can be distinguished. Chemical criteria characterizing these different domains can be identified and are then used to filter the data set to only extract U-Pb age information from portions of the sample that belong to the same genetic domain. Defining data selection criteria in this manner provides more transparency in U-Pb carbonate age data processing as these criteria (and the rationale for their definition) can be reported in the relevant data tables. Moreover, the capability to visually inspect the data set and easily link it with textural and geochemical information greatly assists in the geological interpretation of the U-Pb data. The ability to monitor multiple elements for geochemical sample characterization is particularly suitable for analytical setups that are capable of rapidly or simultaneously scanning over a large mass range with only minor or no settling time (quadrupole ICP-MS, sector field instruments with rapid peak-jumping mode, time-of-flight ICP-MS).

A sufficient spread in U-Pb data points on Tera-Wasserburg concordia or on an isochron plot is an important requirement for successful U-Pb dating of carbonates. The Monocle-based data processing approach adopted here has the advantage over other approaches (e.g., LA-ICP-MS spot analysis or solution-based ICP-MS analysis) in that maximum dispersion along a discordia line or isochron can be retrieved from the data set by stepped pooling of the individual pixels using a proxy for the parent/daughter ratio (Figures 1e and 2f).

Nevertheless, there are still samples with Pb/U ratios that are too homogeneous and/or too high to derive a well-constrained regression line or isochron. Even in the case of samples with high proportions of radiogenic Pb that plot close to the lower intercept on Tera-Wasserburg concordia, it may be impossible to obtain a well-constrained U-Pb date without independent knowledge of the initial Pb composition. Furthermore, the large analyte volume (i.e., large spot size) required in U-Pb dating of low U materials such as carbonates puts a limit on the resolution of the image maps. This may be a problem in fine-grained carbonate rocks with multiple age components (e.g., carbonate clasts within a carbonate cement or carbonate rocks with different generations of thin cements). In such cases the majority of the pixel data may represent mixtures between different textural domains, but this spatial resolution issue clearly also applies to other U-Pb carbonate dating methods (e.g., LA-ICP-MS spot analysis or solution-based approaches).

A clear advantage of the image mapping approach is the ability to pool nonadjacent pixels (e.g., Figure 1d), as opposed to selecting contiguous data points from the time-resolved signal or employing data points composed of individual spot analyses. In this study it was found that pooling of pixels corresponding to between ~30 and 60 s of signal was sufficient for a well-constrained data point on a Tera-Wasserburg concordia or isochron plot. However, the optimum signal length for a well-constrained data point is dependent on a variety of factors. These include (i) the U concentration and the age of the sample which both determine the amount of ingrowth of radiogenic Pb; (ii) the number of pixels in the data set (i.e., the target domain area on the image map); and (iii) the range and pattern of the cumulative distribution curve of the pooling channel which is a proxy for the $^{238}U/^{206}Pb$ parent/daughter ratio.

Despite the advantages of the Monocle-based approach, a "black-box" application of the method can result in inaccurate age determinations. Domains characterized by detrital contamination, authigenic carbonate growth, or local resetting of the U-Pb system due to postformational fluid ingress are not always evident on Tera-Wasserburg concordia or isochron plots once the stepped pooling of pixels procedure has been undertaken. Detailed sample characterization combined with monitoring the spatial distributions of a suite of major and trace elements must be undertaken first to make the image mapping technique a powerful and transparent tool for LA-ICP-MS U-Pb dating of carbonates. After identification and isolation of potentially different genetic domains, several tests can be undertaken to check the accuracy and consistency of the U-Pb data derived from Monocle-based selection and pooling of pixels and to avoid inaccurate age determinations resulting from data processing artifacts. Coherent behavior of the data points on Tera-Wasserburg concordia, $^{206}Pb/^{208}Pb_{common}$ versus $^{238}U/^{208}Pb_{common}$ isochron, and $^{208}Pb_{common}/^{206}Pb_{total}$ versus $^{238}U/^{206}Pb_{total}$ (86TW in the sense of Parrish et al., 2018) plots is essential and must yield consistent (i.e., within analytical uncertainty) U-Pb dates and initial Pb compositions. These results should also be compared to those derived from conventional (i.e., manual) selections made from the time-resolved signal.

6. Conclusions

The image mapping approach to LA-ICP-MS U-Pb dating of carbonates presented here is based on selection and pooling of pixels from 2-D elemental and isotopic ratio maps. It represents an effective tool for inspection, filtering, and statistical treatment of data sets acquired by quadrupole ICP-MS but is also applicable to other instruments (TOF, single collector sector field ICP-MS, and ICP-MS/MC-ICP-MS split stream setups). In addition to the acquisition of U-Pb isotope data, several major and trace elements are monitored to assist in revealing mineralogical variation, the presence of detrital material or other inhomogeneities (e.g., veins or diagenetic cements), and detecting postformational fluid ingress. Such features are important in identifying and isolating domains that are potentially of different age or are unsuitable for U-Pb dating. Each data point of the time-resolved signal is translated into one pixel on the image map using the map interrogation tool Monocle. The image maps can be constructed for elements, elemental ratios, or isotopic ratios. These maps can be precisely placed over photomicrographs, cathodoluminescence, or SEM images of the sample, allowing for rapid visual inspection and evaluation of the geochemical and U-Pb data in combination with structural, textural, and mineralogical features. After careful inspection and evaluation, pixels from the maps can be selected according to certain criteria to target and select textural domains that are likely homogeneous in age. The pixels within the selected domain are then pooled into a set of analyses using a proxy for the $^{238}U/^{206}Pb$ ratio to retrieve the largest possible spread of the data points on Tera-Wasserburg concordia or isochron diagrams. The application of robust

filtering criteria for selecting data is more transparent than other data processing procedures as the sample-specific filtering criteria and their rationale can be reported. This image mapping approach is ideally suited for generating and interpreting accurate and precise U-Pb LA-ICP-MS carbonate age data, particularly in carbonate samples with complex geological histories.

Acknowledgments
The study was supported by a Science Foundation Ireland grant (15/IA/3024) that is partly funded by the Geological Survey of Ireland and the Environmental Protection Agency, Ireland. J. A. P. acknowledges a Natural Sciences and Engineering Research Council of Canada (NSERC) postdoctoral fellowship PDF-487902-2016. Carol A. Hill and Victor J. Polyak are thanked for kindly providing a sample of the Long Point Limestone. We appreciate the constructive comments of reviewer Nick Roberts and the editorial handling by Janne Blichert-Toft. The full data tables for analyses presented in this study are provided in supporting information Data Set S1.

References

Babinski, M., Chemale, F., & Van Schmus, W. R. (1995). The Pb/Pb age of the Minas Supergroup carbonate rocks, Quadrilátero Ferrífero, Brazil. *Precambrian Research*, *72*(3-4), 235–245. https://doi.org/10.1016/0301-9268(94)00091-5

Brand, U., & Veizer, J. (1980). Chemical diagenesis of a multicomponent carbonate system; 1, Trace elements. *Journal of Sedimentary Research*, *50*(4), 1219–1236.

Burisch, M., Gerdes, A., Walter, B. F., Neumann, U., Fettel, M., & Markl, G. (2017). Methane and the origin of five-element veins: Mineralogy, age, fluid inclusion chemistry and ore forming processes in the Odenwald, SW Germany. *Ore Geology Reviews*, *81*, 42–61. https://doi.org/10.1016/j.oregeorev.2016.10.033

Chew, D. M., Petrus, J. A., & Kamber, B. S. (2014). U–Pb LA–ICPMS dating using accessory mineral standards with variable common Pb. *Chemical Geology*, *363*(Supplement C), 185–199. https://doi.org/10.1016/j.chemgeo.2013.11.006

Coogan, L. A., Parrish, R. R., & Roberts, N. M. W. (2016). Early hydrothermal carbon uptake by the upper oceanic crust: Insight from in situ U-Pb dating. *Geology*, *44*(2), 147–150. https://doi.org/10.1130/G37212.1

Denniston, R. F., Asmerom, Y., Polyak, V. Y., McNeill, D. F., Klaus, J. S., Cole, P., & Budd, A. F. (2008). Caribbean chronostratigraphy refined with U-Pb dating of a Miocene coral. *Geology*, *36*(2), 151. https://doi.org/10.1130/G24280A.1

Duffin, A. M., Springer, K. W., Ward, J. D., Jarman, K. D., Robinson, J. W., Endres, M. C., et al. (2015). Femtosecond laser ablation multicollector ICPMS analysis of uranium isotopes in NIST glass. *Journal of Analytical Atomic Spectrometry*, *30*(5), 1100–1107. https://doi.org/10.1039/C4JA00452C

Eggins, S. M., & Shelley, J. M. G. (2002). Compositional heterogeneity in NIST SRM 610-617 glasses. *Geostandards Newsletter*, *26*(3), 269–286. https://doi.org/10.1111/j.1751-908X.2002.tb00634.x

Eichwald, E. (1829). Zoologia Specialis. Pars prior. Vilnae: J. Zawadzki.

Flügel, E. (2010). 7. Diagenesis, porosity, and dolomitization. In *Microfacies of carbonate rocks: Analysis, interpretation and application*, (pp. 267–338). Berlin, Heidelberg: Springer.

Gebhardt, U. (1988). Mikrofazies und Paläontologie biogener Karbonate der Unteren Mansfelder Schichten (Oberkarbon, Stefan). *Hallesches Jahrbuch für Geowissenschaften*, *13*, 5–21.

Gebhardt, U., & Schneider, J. W. (1985). Stomochara aus den Mansfelder Schichten (Stefan) der Saale-Senke und der erste sichere Nachweis von Characeen-Thalli im Paläozoikum. *Freiberger Forschungshefte C*, *400*, 37–43.

Getty, S. R., Asmerom, Y., Quinn, T. M., & Budd, A. F. (2001). Accelerated Pleistocene coral extinctions in the Caribbean Basin shown by uranium-lead (U-Pb) dating. *Geology*, *29*(7), 639–642. https://doi.org/10.1130/0091-7613(2001)029<0639:APCEIT>2.0.CO;2

Godeau, N., Deschamps, P., Guihou, A., Leonide, P., Tendil, A., Gerdes, A., et al. (2018). U-Pb dating of calcite cement and diagenetic history in microporous carbonate reservoirs: Case of the Urgonian limestone, France. *Geology*, *46*(3), 247–250. https://doi.org/10.1130/G39905.1

Hansman, R. J., Albert, R., Gerdes, A., & Ring, U. (2018). Absolute ages of multiple generations of brittle structures by U-Pb dating of calcite. *Geology*, *46*(3), 207–210. https://doi.org/10.1130/G39822.1

Hill, C. A., Polyak, V. J., Asmerom, Y., & Provencio, P. (2016). Constraints on a Late Cretaceous uplift, denudation, and incision of the Grand Canyon region, southwestern Colorado Plateau, USA, from U-Pb dating of lacustrine limestone. *Tectonics*, *35*, 896–906. https://doi.org/10.1002/2016TC004166

Hints, L. (2014). Revision of the concept of the orthide brachiopod Cyrtonotella in the Middle Ordovician of the East Baltic. *Estonian Journal of Earth Sciences*, *63*(2), 63–70. https://doi.org/10.3176/earth.2014.05

Hoff, J. A., Jameson, J., & Hanson, G. N. (1995). Application of Pb isotopes to the absolute timing of regional exposure events in carbonate rocks; an example from U-rich dolostones from the Wahoo formation (Pennsylvanian), Prudhoe Bay, Alaska. *Journal of Sedimentary Research*, *65*(1a), 225.

Hu, Z., Gao, S., Liu, Y., Hu, S., Chen, H., & Yuan, H. (2008). Signal enhancement in laser ablation ICP-MS by addition of nitrogen in the central channel gas. *Journal of Analytical Atomic Spectrometry*, *23*(8), 1093–1101. https://doi.org/10.1039/b804760j

Jahn, B.-M. (1988). Pb/Pb dating of young marbles from Taiwan. *Nature*, *332*(6163), 429–432. https://doi.org/10.1038/332429a0

Jochum, K. P., Weis, U., Stoll, B., Kuzmin, D., Yang, Q., Raczek, I., et al. (2011). Determination of reference values for NIST SRM 610–617 glasses following ISO guidelines. *Geostandards and Geoanalytical Research*, *35*(4), 397–429. https://doi.org/10.1111/j.1751-908X.2011.00120.x

Košler, J., & Sylvester, P. J. (2003). Present trends and the future of zircon in geochronology: Laser ablation ICPMS. *Reviews in Mineralogy and Geochemistry*, *53*(1), 243–275. https://doi.org/10.2113/0530243

Li, Q., Parrish, R. R., Horstwood, M. S. A., & McArthur, J. M. (2014). U–Pb dating of cements in Mesozoic ammonites. *Chemical Geology*, *376*, 76–83. https://doi.org/10.1016/j.chemgeo.2014.03.020

Lindskog, A., Costa, M. M., Rasmussen, C. M. Ø., Connelly, J. N., & Eriksson, M. E. (2017). Refined Ordovician timescale reveals no link between asteroid breakup and biodiversification. *Nature Communications*, *8*, 14066. https://doi.org/10.1038/ncomms14066

Ludwig, K. R. (2012). User's manual for Isoplot 3.75. *Berkley Geochronology Center Special Publication*, *5*, 1–75.

van Malderen, S. J. M., Managh, A. J., Sharp, B. L., & Vanhaecke, F. (2016). Recent developments in the design of rapid response cells for laser ablation-inductively coupled plasma-mass spectrometry and their impact on bioimaging applications. *Journal of Analytical Atomic Spectrometry*, *31*(2), 423–439. https://doi.org/10.1039/C5JA00430F

Moorbath, S., Taylor, P. N., Orpen, J. L., Treloar, P., & Wilson, J. F. (1987). First direct radiometric dating of Archaean stromatolitic limestone. *Nature*, *326*(6116), 865–867. https://doi.org/10.1038/326865a0

Nuriel, P., Weinberger, R., Kylander-Clark, A. R. C., Hacker, B. R., & Craddock, J. P. (2017). The onset of the Dead Sea transform based on calcite age-strain analyses. *Geology*, *45*(7), 587–590. https://doi.org/10.1130/G38903.1

Opluštil, S., Jirásek, J., Schmitz, M., & Matýsek, D. (2017). Biotic changes around the radioisotopically constrained Carboniferous-Permian boundary in the Boskovice Basin (Czech Republic). *Bulletin of Geosciences*, *92*(1), 95–122.

Opluštil, S., Schmitz, M., Cleal, C. J., & Martínek, K. (2016). A review of the Middle–Late Pennsylvanian west European regional substages and floral biozones, and their correlation to the geological time scale based on new U–Pb ages. *Earth-Science Reviews*, *154*, 301–335. https://doi.org/10.1016/j.earscirev.2016.01.004

Opluštil, S., Schmitz, M., Kachlík, V., & Štamberg, S. (2016). Re-assessment of lithostratigraphy, biostratigraphy, and volcanic activity of the late Paleozoic intra-Sudetic, Krkonose-Piedmont and Mnichovo Hradiste basins (Czech Republic) based on new U-Pb CA-ID-TIMS ages. *Bulletin of Geosciences*, *91*(2), 399–432.

Pagel, M., Bonifacie, M., Schneider, D. A., Gautheron, C., Brigaud, B., Calmels, D., et al. (2018). Improving paleohydrological and diagenetic reconstructions in calcite veins and breccia of a sedimentary basin by combining Δ47 temperature, $\delta^{18}O$ water and U-Pb age. *Chemical Geology*, *481*, 1–17. https://doi.org/10.1016/j.chemgeo.2017.12.026

Parrish, R. R., Parrish, C. M., & Lasalle, S. (2018). Vein calcite dating reveals Pyrenean orogen as cause of Paleogene deformation in southern England. *Journal of the Geological Society*, *175*(3), 425–442. https://doi.org/10.1144/jgs2017-107

Paton, C., Hellstrom, J., Paul, B., Woodhead, J., & Hergt, J. (2011). Iolite: Freeware for the visualisation and processing of mass spectrometric data. *Journal of Analytical Atomic Spectrometry*, *26*(12), 2508–2518. https://doi.org/10.1039/c1ja10172b

Paton, C., Woodhead, J. D., Hellstrom, J. C., Hergt, J. M., Greig, A., & Maas, R. (2010). Improved laser ablation U-Pb zircon geochronology through robust downhole fractionation correction. *Geochemistry, Geophysics, Geosystems*, *11*, Q0AA06. https://doi.org/10.1029/2009GC002618

Pellenard, P., Gand, G., Schmitz, M., Galtier, J., Broutin, J., & Stéyer, J.-S. (2017). High-precision U-Pb zircon ages for explosive volcanism calibrating the NW European continental Autunian stratotype. *Gondwana Research*, *51*, 118–136. https://doi.org/10.1016/j.gr.2017.07.014

Petrus, J. A., Chew, D. M., Leybourne, M. I., & Kamber, B. S. (2017). A new approach to laser-ablation inductively-coupled-plasma mass-spectrometry (LA-ICP-MS) using the flexible map interrogation tool 'Monocle'. *Chemical Geology*, *463*, 76–93. https://doi.org/10.1016/j.chemgeo.2017.04.027

Petrus, J. A., & Kamber, B. S. (2012). VizualAge: A novel approach to laser ablation ICP-MS U-Pb geochronology data reduction. *Geostandards and Geoanalytical Research*, *36*(3), 247–270. https://doi.org/10.1111/j.1751-908X.2012.00158.x

Rasbury, E. T., & Cole, J. M. (2009). Directly dating geologic events: U-Pb dating of carbonates. *Reviews of Geophysics*, *47*, RG3001. https://doi.org/10.1029/2007RG000246

Rasbury, E. T., Hanson, G. N., Meyers, W. J., Holt, W. E., Goldstein, R. H., & Saller, A. H. (1998). U-Pb dates of paleosols: Constraints on late Paleozoic cycle durations and boundary ages. *Geology*, *26*(5), 403–406. https://doi.org/10.1130/0091-7613(1998)026<0403:UPDOPC>2.3.CO;2

Reinhold, C. (1998). Multiple episodes of dolomitization and dolomite recrystallization during shallow burial in Upper Jurassic shelf carbonates: Eastern Swabian Alb, southern Germany. *Sedimentary Geology*, *121*(1-2), 71–95. https://doi.org/10.1016/S0037-0738(98)00077-3

Ring, U., & Gerdes, A. (2016). Kinematics of the Alpenrhein-Bodensee graben system in the Central Alps: Oligocene/Miocene transtension due to formation of the Western Alps arc. *Tectonics*, *35*, 1367–1391. https://doi.org/10.1002/2015TC004085

Roberts, N. M. W., Rasbury, E. T., Parrish, R. R., Smith, C. J., Horstwood, M. S. A., & Condon, D. J. (2017). A calcite reference material for LA-ICP-MS U-Pb geochronology. *Geochemistry, Geophysics, Geosystems*, *18*, 2807–2814. https://doi.org/10.1002/2016GC006784

Roberts, N. M. W., & Walker, R. J. (2016). U-Pb geochronology of calcite-mineralized faults: Absolute timing of rift-related fault events on the northeast Atlantic margin. *Geology*, *44*(7), 531–534. https://doi.org/10.1130/G37868.1

Schneider, J. W., Rössler, R., Gaitzsch, B. G., Gebhardt, U., & Kampe, A. (2005). 4.2.4 Saale Senke. *Courier Forschungsinstitut Senckenberg*, *254*, 419–440.

Schneider, J. W., & Scholze, F. (2018). Late Pennsylvanian–Early Triassic conchostracan biostratigraphy: A preliminary approach. *Geological Society, London, Special Publications*, *450*(1), 365–386. https://doi.org/10.1144/SP450.6

Schneider, J. W., & Werneburg, R. (2012). Biostratigraphie des Rotliegend mit Insekten und Amphibien. *Schriftenreihe der Deutschen Gesellschaft für Geowissenschaften*, *61*, 110–142.

Smith, P. E., Farquhar, R. M., & Hancock, R. G. (1991). Direct radiometric age determination of carbonate diagenesis using U-Pb in secondary calcite. *Earth and Planetary Science Letters*, *105*(4), 474–491. https://doi.org/10.1016/0012-821X(91)90186-L

Stacey, J. S., & Kramers, J. D. (1975). Approximation of terrestrial lead isotope evolution by a two-stage model. *Earth and Planetary Science Letters*, *26*(2), 207–221. https://doi.org/10.1016/0012-821X(75)90088-6

Wang, Z. S., Rasbury, E. T., Hanson, G. N., & Meyers, W. J. (1998). Using the U-Pb system of calcretes to date the time of sedimentation of clastic sedimentary rocks. *Geochimica et Cosmochimica Acta*, *62*(16), 2823–2835. https://doi.org/10.1016/S0016-7037(98)00201-4

Woodhead, J., Reisz, R., Fox, D., Drysdale, R., Hellstrom, J., Maas, R., et al. (2010). Speleothem climate records from deep time? Exploring the potential with an example from the Permian. *Geology*, *38*(5), 455–458. https://doi.org/10.1130/G30354.1

Woodhead, J. D., & Hergt, J. M. (2001). Strontium, neodymium and lead isotope analyses of NIST glass certified reference materials: SRM 610, 612, 614. *Geostandards Newsletter*, *25*(2–3), 261–266. https://doi.org/10.1111/j.1751-908X.2001.tb00601.x